Chinese Chemical Letters 37 (2026) 111852

Contents lists available at ScienceDirect

Chinese Chemical Letters

journal homepage: www.elsevier.com/locate/cclet

Gold nanorods-loaded quaternized mesoporous silica nanospheres with synergistic adhesion and photothermal antibacterial mechanism for diabetic wound healing

Kaihang Sheng[a,1], Yanshuai Wang[a,1], Siyuan Yin[a], Xiuling Li[b], Xinya Zhang[a], Xiaowei Li[b,*], Dechao Niu[a,*]

[a] Low Dimensional Materials Chemistry Laboratory, Key Laboratory for Ultrafine Materials of Ministry of Education, Frontier Science Center of the Materials Biology and Dynamic Chemistry, School of Materials Science and Engineering, East China University of Science and Technology, Shanghai 200237, China
[b] School of Materials Science and Engineering, Shandong University of Technology, Zibo 255000, China

ARTICLE INFO

Article history:
Received 24 June 2025
Revised 16 September 2025
Accepted 17 September 2025
Available online 17 September 2025

Keywords:
Antibacterial
Mesoporous silica
Quaternization
Adhesion
Photothermal

ABSTRACT

Synergistic strategy of cationic antibacterial and nanoparticle mediated photothermal conversion provides new opportunities to address bacterial infections. However, the conventional post-modification and lack of precise structural regulation, leads to the complexity of operation and unsatisfying synergistic effect on antibacterial performance. To address these challenges, herein, a novel "selective extraction and domain-restricted growth" approach has been proposed to successfully synthesize quaternized mesoporous silica nanosphere (QMSN) encapsulating gold nanorods (GNRs) inside the pore channel (GNRs@QMSN) for the treatment of bacterial infected diabetic wound. The strategy exhibits extensive convenience, enabling the ultra-uniform microporous core-mesoporous shell structure with positive charges. Most importantly, GNRs@QMSN demonstrated an excellent photothermal conversion efficiency up to 63.73%, due to the unique pore-domain-limited effect. Under the synergistic effect of positive charge surface for enhanced bacteria adhesion, intrinsic antibacterial quaternization and GNRs-mediated photothermal conversion, GNRs@QMSN exhibited excellent antibacterial and antibiofilm performance *in vitro*. The feasibility of GNRs@QMSN was further validated in a mouse diabetic wound infection model. This novel QMSN encapsulating GNRs is expected to be a promising paradigm for bacterial infected wound healing.

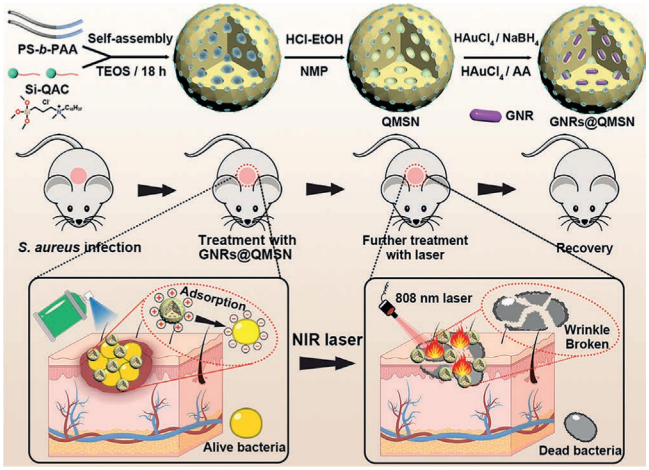
© 2026 Published by Elsevier B.V. on behalf of Chinese Chemical Society and Institute of Materia Medica, Chinese Academy of Medical Sciences.

Diabetic chronic wounds are prone to bacterial infections [1,2]. The high sugar environment weakens the immune response, resulting in an infection rate of over 60% [3], which severely hinders tissue regeneration. Traditional antibiotic therapy faces severe challenges [4,5]: On one hand, drug-resistant bacteria (such as methicillin-resistance *Staphylococcus aureus* (MRSA)) and biofilm formation significantly reduce the efficacy of drugs; on the other hand, systemic medication has problems such as poor targeting, insufficient local concentration, and is prone to causing liver and kidney toxicity. It is urgent to develop new antibacterial strategies that are both highly effective in killing bacteria and safe in terms of biological safety.

Over the past decades, advances in nanomaterial mediated antibiotic-free antibacterial strategies provide new opportunities to address these challenges [6–10]. Among them, silica-based materials are regarded as ideal antibacterial drug carriers due to their excellent chemical stability and biocompatibility [11–13], *etc*. However, conventional silica-based materials lack intrinsic antibacterial activity and must be loaded with antibacterial actives (nanoenzymes, photosensitizers, and antibacterial drugs, *etc*.) or post-modified to achieve antibacterial effects. Tao *et al*. constructed a bifunctionalized mesoporous silica nanoparticles (MSN-AuNPs), which possesses dual enzyme activities similar to those of peroxidases and oxidases at the same time, by generating reactive oxygen species (ROS) to efficiently kill bacteria and destroy biofilms [14]. Cao *et al*. prepared Ag-Bi@SiO_2 nanoparticles (NPs) by an *in-situ* growth method. The obatined Ag-Bi@SiO_2 NPs can accelerate the release of Ag^+ through photothermal effect, and the local high temperature synergistically damages the cell membrane and biofilm of bacteria [15]. Xin *et al*. prepared a novel nano-acoustic sensitized agent (DT-Ag-CS+) by growing TiO_2 on dendritic macroporous meso–silica nanoparticles, then depositating Ag, and modifying it with quaternary ammonium chitosan (CS+), which induces

* Corresponding authors.
E-mail addresses: weis.lee@163.com (X. Li), dcniu@ecust.edu.cn (D. Niu).
[1] These authors contributed equally to this work.

https://doi.org/10.1016/j.cclet.2025.111852
1001-8417/© 2026 Published by Elsevier B.V. on behalf of Chinese Chemical Society and Institute of Materia Medica, Chinese Academy of Medical Sciences.



Scheme 1. Schematic diagram of the synthesis process and the application of GNRs@QMSN for wound infection.

the production of ROS through both sonodynamic and chemodynamic effects, thereby destroying the periodontal pathogenic bacteria *Porphyromonas gingivalis* and its biofilm [16]. Although these functionalized modifications can partially enhance the antibacterial performance of the silica-based materials, the complex post-modification steps undoubtedly increase the cost of the operation. In addition, existing technologies lack the integrated design of dual-acting synergistic bactericidal and targeting enhancement, which becomes a key obstacle to achieve long-lasting and broad-spectrum antibacterial effects.

Herein, a facile "selective extraction and domain-restricted growth" approach has been proposed to successfully synthesize a quaternized mesoporous silica nanosphere (QMSN) with high positive potential and macroporous structure, uniting with gold nanorods (GNRs) for adhesion, intrinsic and synergistic photothermal treatment of diabetic wound infection (Scheme 1). QMSN was synthesized by self-assembly of two organic templating agents, anionic block copolymer polystylene-*b*-polyacrylic acid (PS-*b*-PAA) and dimethyloctadecyl (3-(trimethoxysilyl)propyl)ammonium chloride (Si-QAC), in the presence of tetraethyl orthosilicate, thereafter selectively extracting by *N*-methylpyrrolidone (NMP) to remove the templating agent PS-*b*-PAA. Subsequently, GNRs were loaded *in situ* into the pores of QMSN using the confined gold seed-growth method to prepare the QMSN encapsulating GNRs (GNRs@QMSN). QMSN has a uniform "microporous core-small pore shell" spherical structure. Interestingly, the aspect ratio and longitudinal plasmon resonance absorption peaks of the loaded GNRs can be tuned by simply varying the amount of chloroauric acid ($HAuCl_4$) in the growth solution. In addition, mesoporous silica nanosphere (MSN) without Si-QAC was prepared by post-calcination treatment, while mesoporous silica encapsulating GNRs (GNRs@MSN) was prepared using the same gold seed-growth method as a control. GNRs@QMSN shown good dispersion in various solvents with a photothermal conversion efficiency up to 63.73%. Meanwhile, GNRs@QMSN exhibited good biocompatibility against mammalian cells. Compared with GNRs@MSN, the surface of GNRs@QMSN was positively charged. Under the synergistic effect of positive charge surface, intrinsic antibacterial quaternization and GNRs mediated photothermal conversion, GNRs@QMSN exhibited excellent antibacterial and anti-biofilm performance *in vitro*. Furthermore, the feasibility of GNRs@QMSN for bacterial infection treatment was verified *in vivo* by a rat model of diabetic co-infection.

QMSN was prepared as illustrated in Fig. 1a. In detail, PS_{140}-*b*-PAA_{18} and Si-QAC were self-assembled into micelles in tetrahydrofuran solution, where the small-pore templating agent was Si-QAC mono-micelles and the large-pore templating agent was a composite micelle of PS_{140}-*b*-PAA_{18} and Si-QAC. The micelles were replicated by introducing the inorganic precursor tetraethyl orthosilicate, and the resulting QMSN samples were finally obtained through selectively extracting by NMP to remove the templating agent PS_{140}-*b*-PAA_{18}. In order to prepare QMSN with homogeneous morphology and well-defined pores, the parameters were adjusted. In order to prepare QMSN with homogeneous morphology and regular pore structure, a series of QMSNs were synthesized by adjusting the amount of Si-QAC, the segments of PS-*b*-PAA, temperature, aging method and the amount of $NH_3{\cdot}H_2O$. Notably, the shell layer of QMSN was controllably varied from 21.2 nm to 41.3 nm with the increase amount of Si-QAC from 10 mg to 50 mg (Fig. S1 in Supporting information). It was attributed to the fact that the large mesoporous region of QMSN was co-constructed by the composite micelles of PS_{140}-*b*-PAA_{18} and Si-QAC, while the small mesoporous shell layer originates from the interaction of single Si-QAC micelle with the silica source. When the amount of Si-QAC increases, the thicker shell layer of QMSN is formed. The structure and pores of QMSN tended to be ordered as the $NH_3{\cdot}H_2O$ was increased from 0.25 mL to 1.5 mL (Fig. S2 in Supporting information), it was attributed to the fact that hydrolysis reaction rate is accelerated by an increase in ammonia concentration, and the hydrolysis of tetraethyl orthosilicate (TEOS) tends to synchronize with the self-assembly of the templating agent, leading to a homogeneous arrangement of the pores [17–19]. In addition, the effects of temperature, chain segments of PS-*b*-PAA and aging method on the structure of QMSN have been also explored, and the various characterizations are shown in Figs. S3–S5 (Supporting information), we found that temperature [20,21] and aging mode [22–24] mainly affect the pore structure of QMSN, and the chain segment of PS-*b*-PAA affects its shell structure [25]. It is noteworthy that the size, hydrodynamic diameter and zeta potential of the QMSN did not fluctuate much with each parameter during the synthesis process (Figs. 1b–k).

As a control, mesoporous silica with Si-QAC removed (MSN) was prepared by calcination. QMSN and MSN were characterized and tested by various methods. As shown in Fig. S6 (Supporting information), the hydrodynamic diameter of QMSN and MSN are ~250 nm as measured by dynamic light scattering. Fourier transform infrared (FT-IR) spectra of QMSN and MSN were recorded to demonstrate the retention of quaternary ammonium ions in QMSN (Fig. 1l). Compared with MSN, QMSN shown distinct absorption peaks at 2800–3000, 1590–1690 and 1300–1500 cm^{-1}, which correspond to the C–H stretching vibration peak, the C–N stretching vibration peak and the C–H bending vibration peak, respectively, confirming the successful retention of quaternary ammonium ions in QMSN. Besides, the zeta potential (Fig. 1m) results shown that the surface of QMSN exhibited a highly positive potential. On the contrary, calcination removes Si-QAC, leaving the MSN negatively charged. The chemical compositions and functional groups of QMSN have also been investigated by X-ray photoelectron spectroscopy (XPS). As shown by the high-resolution XPS curve, C–N, N–Cl, Si-O and C-Si chemical bonds exist in QMSN (Figs. S7a and b in Supporting information). In addition, nitrogen sorption isotherms of the obtained QMSN display representative type-IV curves with a rapid increase in the adsorption branch at a relative pressure of 0.7 to 0.9, indicating the presence of uniform mesopores (Fig. S8 in Supporting information). The Brunauer-Emmett-Teller (BET) surface area and pore area were calculated to be as high as 154.23 m^2/g and 0.40 cm^3/g, respectively.

In order to construct material systems for adhesion and photothermal synergistic antibacterial, QMSN encapsulating GNRs inside the pore channel have been further synthesized using the core-shell structure of QMSN as a nanoreactor, and employing the "domain-restricted growth" strategy previously developed by our

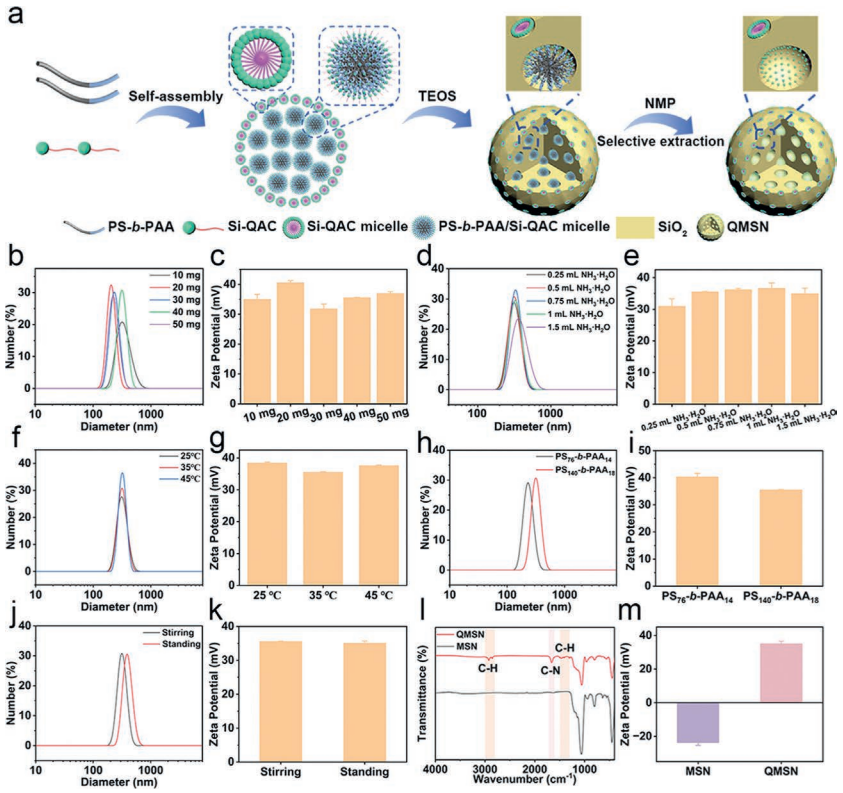


Fig. 1. (a) Schematic synthesis of QMSN prepared by selective extraction strategy. Hydrodynamic diameters (b) and zeta potentials (c) of QMSN obtained by changing the amount of Si-QAC. Hydrodynamic diameters (d) and zeta potentials (e) of QMSN obtained by changing the amount of $NH_3{\cdot}H_2O$. Hydrodynamic diameters (f) and zeta potentials (g) of QMSN obtained by changing temperature. Hydrodynamic diameters (h) and zeta potentials (i) of QMSN obtained by changing the segments of PS-*b*-PAA. Hydrodynamic diameters (j) and zeta potential (k) of QMSN obtained by changing aging mode. (l) FT-IR spectra of QMSN and MSN. (m) Zeta potentials of QMSN and MSN. Data are presented as mean ± standard deviation (SD) ($n = 3$).

group [26]. As a control, CTAB-stabilized GNRs (CTAB-GNRs) were prepared by the same method. As shown in Fig. S9 (Supporting information), CTAB-GNRs exhibit a rod-like particle morphology, with positively charged surfaces, and their hydrated size is approximately 28 nm (Figs. S10 and S11 in Supporting information). It noted that Au seeds played a crucial role in the synthesis process of GNRs@QMSN, as shown in Fig. S12 (Supporting information), the formation of gold seeds occurs within the large pores rather than in the small pores of QMSN. After domain-restricted growth, GNRs@QMSN still maintained a spherical morphology (Fig. 2a and Fig. S13 in Supporting information) and high-resolution transmission electron microscope (TEM) image (Fig. 2b) shown that GNRs@QMSN has high crystallinity, with the crystal face spacing of 0.14 and 0.20 nm corresponding to the (220) and (200) crystal faces of Au, respectively. Moreover, the distribution of Si, O, N and Au elements in the GNRs@QMSN is shown in the dark-field TEM image and the corresponding energy dispersive spectroscopy (EDS) elemental mapping results in Fig. 2c. In addition, the successful loading of GNRs is also demonstrated by the X-ray diffraction (XRD) pattern of GNRs@QMSN (Fig. 2d).

The chemical compositions and functional groups of GNRs@QMSN have been investigated by XPS. As shown by the high-resolution XPS curve, C–N, N–Cl, Si-O and C-Si chemical bonds were also existed in GNRs@QMSN (Figs. S14a and b in Supporting information). As shown in Fig. S14c (Supporting information), the Au 4f spectrum of GNRs@QMSN has two peaks at 84 and 87.7 eV, which are attributed to $4f_{7/2}$ and $4f_{5/2}$ of Au^0, respectively. The total XPS curves of GNRs@QMSN (Fig. S14d in Supporting information) shown that there are C, O, Si and N elements in NPs, and the presence of Au element attests to the successful loading of GNRs. The hydrodynamic diameters distribution (Fig. S10) of GNRs@QMSN and GNRs@MSN show that after loading GNRs, the particle size of the material is around 255 nm and the GNRs@QMSN still maintains high positive potentials (Fig. S11). The pore structure of GNRs@QMSN is similar to that of QMSN (Fig. 2e), indicating that the reduction process does not have a significant effect on the pore structure and pore parameters of QMSN. The BET surface area and pore area decreased to 83.05 m^2/g and 0.19 cm^3/g, respectively, indicated the successful loading of GNRs. The loading content of GNRs in QMSN is 35 % in weight. The good biostability of GNRs@QMSN in water, phosphate buffered saline (PBS) and DMEM media was demonstrated in Fig. 2f.

Notably, the aspect ratio and longitudinal plasmon resonance absorption peaks of the GNRs@QMSN can be modulated by simply changing the amount of $HAuCl_4$ in the growth solution. As shown in Fig. S15 (Supporting information), when the amount of $HAuCl_4$ was increased from 1.5 mL to 7.5 mL, the gold nanoparticles gradually changed to rods, and when the amount of $HAuCl_4$ was continued to be increased to 9 mL, the gold exhibits the larger particles. Furthermore, the visible-near-infrared (Vis-NIR) spectra of GNRs@QMSN exhibit a change from a single peak to a double peak to a single peak (Fig. S16 in Supporting information).

Before evaluating the photothermal effect of GNRs@QMSN, the Vis-NIR absorption spectra of GNRs@MSN and GNRs@QMSN were recorded separately. Significant absorption peaks centered at 530 and 690 nm can be observed for GNRs@MSN and GNRs@QMSN (Fig. 2g), while the color of the solution changes from pink to purple, indicating the successful growth of GNRs inside the pores. Subsequently, the temperature increment of GNRs@QMSN was monitored under 808 nm laser irradiation at different concentrations and laser power densities. As shown in Figs. 2h and i, the temperature increases more rapidly with increasing GNRs@QMSN concen-

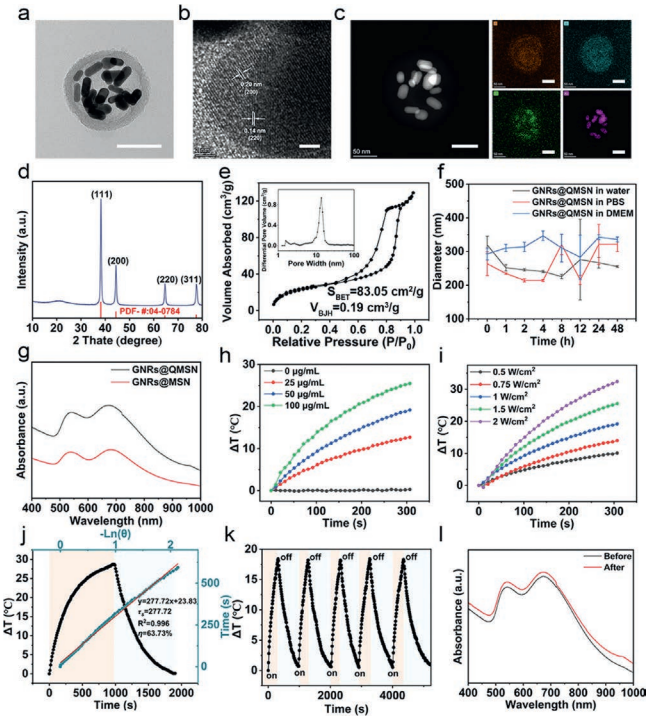


Fig. 2. (a) TEM image of GNRs@QMSN. Scale bar: 200 nm. (b) High-resolution TEM image of GNRs@QMSN. Scale bar: 2 nm. (c) Corresponding elemental mapping images of GNRs@QMSN. Scale bar: 50 nm. (d) XRD pattern of GNRs@QMSN. (e) Nitrogen adsorption–desorption isotherms, pore size distribution of GNRs@QMSN. (f) Diameter stability of GNRs@QMSN dispersed in water, PBS and DMEM media. (g) Vis-NIR absorption spectra of GNRs@MSN and GNRs@QMSN. (h) Photothermal heating curves of GNRs@QMSN with different concentrations. (i) Photothermal heating curves of GNRs@QMSN at varied laser power densities. (j) The photothermal conversion efficiency of GNRs@QMSN. (k) Photothermal heating curves of GNRs@QMSN after five cycles. (l) Vis-NIR absorption spectra of GNRs@QMSN after five cycles. Data are presented as mean ± SD ($n = 3$).

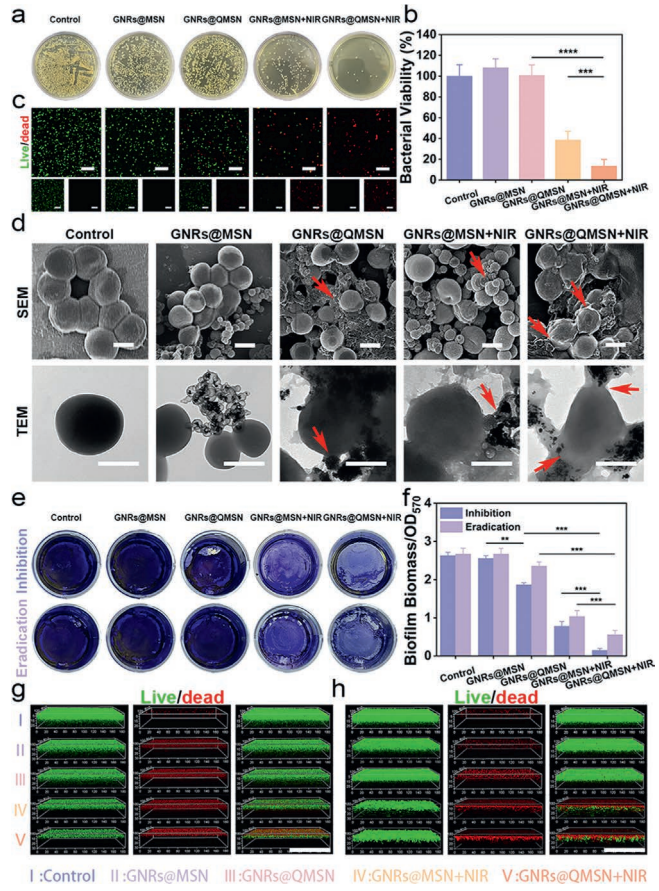


Fig. 3. (a) Digital photographs of *S. aureus* and *E. coli* (10^8 CFU/mL) colonies after treatment with different materials. (b) Bacterial activity of *S. aureus* and *E. coli* (10^8 CFU/mL) treated with different materials. (c) Live/dead staining images of *S. aureus* after treatment with different materials. Scale bar: 20 μm. (d) SEM and TEM images of *S. aureus* after treatment with different materials. Scale bar: 400 nm. (e) Digital photographs of crystal violet staining of different materials after inhibition and eradication of *S. aureus* biofilm. (f) Biomass of *S. aureus* biofilm after treatment with different materials. (g) Three-dimensional confocal fluorescence images of different materials after co-incubation with *S. aureus* biofilm. (h) Three-dimensional confocal fluorescence images of *S. aureus* biofilm after treatment with different materials. Scale bar: 90 μm. Statistical significance was calculated by one-way ANOVA using the Tukey post-test. NIR: 808 nm, 10 min, 1.0 W/cm^2. $^*P < 0.05$, $^{**}P < 0.01$, $^{***}P < 0.001$, $^{****}P < 0.0001$. Data are presented as mean ± SD ($n = 5$).

tration and laser power density, indicating that the photothermal performance of GNRs@QMSN is dependent on both concentration and power. According to the temperature curve and time linear fitting constants (Fig. 2j), the photothermal conversion efficiency of GNRs@QMSN was calculated to be 63.73 %, which was higher than that of other GNRs-based photothermal agents (Table S1 in Supporting information). In addition, no degradation of the photothermal performance of GNRs@QMSN was detected in five consecutive heating/cooling cycles (Fig. 2k), and the corresponding Vis-NIR absorptivity (Fig. 2l) slightly decreased after five heating and cooling cycles, which confirmed the excellent photothermal stability of GNRs@QMSN.

The toxicity of GNRs@QMSN on L929 mouse fibroblast cells was examined prior to the antibacterial activity study. As shown in Fig. S17 (Supporting information), >80 % cell survival was found even at a concentration of 75 μg/mL of Au, indicating that GNRs@QMSN have good cytocompatibility. The quaternary ammonium ions on the surface of GNRs@QMSN are expected to enhance the efficacy of subsequent photothermal therapy (PTT) by adhering to bacteria. To verify this conjecture, two bacteria, *Staphylococcus aureus* (*S. aureus*) and *Escherichia coli* (*E. coli*), were selected as representatives of Gram-positive and Gram-negative bacteria, respectively. As shown in Fig. S18 (Supporting information), the bacterial viability of *S. aureus* and *E. coli* was significantly decreased by 20.7 % and 16.2 %, respectively, when the Au concentration of GNRs@QMSN was 50 μg/mL. In addition, GNRs@QMSN still exhibited excellent inhibitory effects on bacteria even after 72 h (Fig. S19 in Supporting information). After calculation [27], the combination index (CI) for *S. aureus* was 0.9 and for *E. coli* was 0.8, indicating that quaternized GNRs@QMSN and Au-mediated PTT have a synergistic inhibitory effect on bacteria (Fig. S20 in Supporting information).

The effects of GNRs@QMSN on the growth of the two bacteria were evaluated by using the colony formation assay. As shown in Fig. 3 and Fig. S21 (Supporting information), GNRs@MSN alone did not possess significant antibacterial activity (Fig. 3a and Fig. S21a). On the contrary, GNRs@QMSN exhibited a slight inhibitory effect on bacterial proliferation. In addition, NIR irradiation of GNRs@MSN-mediated PTT exhibited a moderate antibacterial effect. Notably, bacteria pretreated with GNRs@QMSN lost the ability to form colonies on agar plates after laser irradiation, *S. aureus* and *E. coli* activities after treatment were 5.9 % and 3.6 % (Fig. 3b and Fig. S21b), respectively, and this excellent bactericidal efficacy was closely related to the adhesive properties and good photothermal performance of GNRs@QMSN. To further evaluate the bacterial inhibition effect of GNRs@QMSN, the treated bacterial samples were stained with Calcein AM/PI staining solution. The results (Fig. 3c and Fig. S21c) showed that GNRs@QMSN effectively killed the bacteria under the irradiation of NIR, and the strong red fluorescence of the propidium iodide (PI) probe was shown, indi-

cating dead bacteria. In contrast, the dominant fluorescence observed in the bacteria with GNRs@QMSN alone was still green, and a small amount of green fluorescence was still observed even after GNRs@MSN + NIR treatment. Bacterial damage can be visualized more visually with scanning electron microscope (SEM) images. As shown in Fig. S22 (Supporting information), it can be seen that the binding efficiency of GNRs@QMSN to bacteria is higher than that of GNRs@MSN. Normally, *S. aureus* was smooth and spherical, while *E. coli* was rod-shaped, however, after treatment, the bacterial surface appeared collapsed and wrinkled, indicating that the bacterial membrane was severely damaged (Fig. 3d and Fig. S21d). This validated the synergistic antibacterial mechanism of quaternized GNRs@QMSN adhesion and photothermal therapy.

Bacterial biofilms are bacteria that attach themselves to inert or active substances in order to adapt to their living conditions, giving them a growth pattern similar to that of planktonic cells [28]. Due to the excellent *in vitro* antibacterial effect of GNRs@QMSN, we have also conducted experiments to investigate its resistance to biofilms. Firstly, the eradication and inhibition effect of GNRs@QMSN on *S. aureus* biofilms was investigated by crystal violet staining experiment. It can be seen that the biofilm of the control group was dense and thick, while the biofilm treated with GNRs@QMSN + NIR was sparse and thin with light purple color (Fig. 3e). Interestingly, GNRs@QMSN also inhibited *S. aureus* biofilm formation in the absence of NIR irradiation (Figs. 3e and f), which may be caused by GNRs@QMSN adsorbing on the bacterial surface *via* positive charge, it was also evident from the plate coating experiment that the number of viable bacteria in the biofilm treated with GNRs@QMSN was significantly reduced (Fig. S23 in Supporting information). In addition, the cell density of the biofilm after different treatments was qualitatively analyzed by SEM, and it was found that bacteria in the GNRs@QMSN, GNRs@MSN + NIR and GNRs@QMSN + NIR groups all appeared to be wrinkled, but those in the GNRs@QMSN + NIR group appeared to be broken between them and the extracellular polymers broke into fragments (Fig. S24 in Supporting information).

Given the smaller size of GNRs@QMSN and the presence of surface quaternary ammonium ions, it is expected to penetrate the mature biofilm matrix and reach the bottom of the matrix [29,30], and in order to validate this conjecture, the biofilm was stained with the calcein AM/PI kit, and confocal fluorescence images of the biofilm were recorded. As can be seen in Fig. 3g, GNRs@QMSN + NIR exhibited good biofilm inhibitory activity, since only a thin biofilm consisting of live bacterial cells can be observed after NIR irradiation. Although there was no significant difference in biofilm thickness between the control and GNRs@QMSN-treated groups, almost all the cells in the GNRs@QMSN + NIR-treated group were dead (Fig. 3h).

In view of the good biofilm eradication effect of GNRs@QMSN as well as the good biosafety *in vitro*, we established a mouse wound infection model by introducing *S. aureus* into the wound site of Sprague Dawley male rats, the schematic diagram (Fig. 4a) depicts the formation of a diabetic wound infection model, and the associated treatment and observation. All animal procedures were performed in accordance with the Guidelines for Care and Use of Laboratory Animals of East China University of Science and Technology, and the experiments were approved by the Animal Ethics Committee of East China University of Science and Technology. The mouse model was randomly divided into five groups: (1) Control, (2) GNRs@MSN, (3) GNRs@QMSN, (4) GNRs@MSN + NIR, (5) GNRs@QMSN + NIR. Treatments were carried out on days 1, 3, and 5 respectively, we took photographs of wounds with different treatments on days 1, 3, 5, and 10, and analyzed the wound healing rate by calculating the size of the relative repair area. After 10 days of treatment, the wound of the mice treated with GNRs@QMSN recovered to the original 3.7%, which proved the excellent wound healing ability of GNRs@QMSN under NIR irradiation. (Figs. 4b–d), In addition, we further evaluated the antibacterial effects of various treatments on the tenth day. The relative percentages of viable bacteria in the GNRs@MSN + NIR group and GNRs@QMSN + NIR group were 38% and 13% (Figs. 4e and f), respectively. The effect of the different treatments on wound healing was further evaluated by histological analysis, and the histological images of skin hematoxylin-eosin (H&E) and Masson stains collected on day 10 (Fig. 4g) shown that the two groups using NIR had intact skin tissue structure, abundant fibroblasts, and fewer neutrophils compared to the two groups not using NIR. Finally, H&E staining was performed on the major organs (heart, liver, spleen, lungs, and kidneys) of the rats. No significant inflammation and edema were seen in the H&E stained images, indicating that GNRs@QMSN did not cause significant tissue damage and had a good biosafety profile (Fig. S25 in Supporting information). Thus, GNRs@QMSN is a promising photothermal antibacterial agent that shows great potential in the treatment of bacterial wound infections.

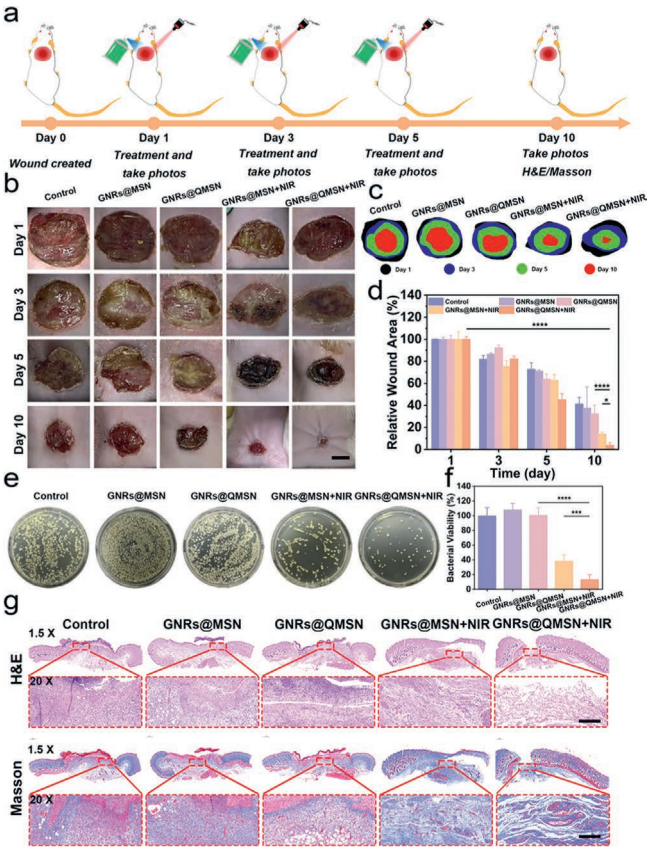


Fig. 4. Potential application of GNRs@QMSN in the treatment of *S. aureus* infections. (a) Establishment of wound infection model and treatment scheme. Digital photographs (b) and healing of wounds (c) in mice after treatment with different materials. Scale bar: 5 mm. (d) Quantitative analysis of the wound area ($n = 3$). Digital photographs of skin wound colonies (e) and statistics on the number of colonies (f) in each group of mice on day 10 ($n = 5$). (g) H&E and Masson staining of wound tissue after treatment with different groups on day 10. Scale bar: 200 μm. Statistical significance was calculated by one-way ANOVA using the Tukey post-test. NIR: 808 nm, 1.0 W/cm^2, 10 min. $^*P < 0.05$, $^{***}P < 0.001$, $^{****}P < 0.0001$. Data are presented as mean ± SD.

In conclusion, we have successfully synthesized QMSN by a simple one-step selective extraction strategy and domain-restricted growth of GNRs *in situ* within the pore channels (termed GNRs@QMSN), which possessed an adhesion, intrinsic and photothermal synergistic treatment of diabetic wound infection. Interestingly, the longitudinal surface plasmon resonance peaks of the GNRs can be modulated by adjusting the amount of chloroau-

ric acid in the reaction solution due to the unique pore-domain-limited effect of QMSN. Under the synergistic effect of positive charge surface for enhanced bacteria adhesion, intrinsic antibacterial quaternization and GNRs mediated photothermal conversion, GNRs@QMSN exhibited excellent antibacterial activity and effectively inhibited the formation of *S. aureus* biofilm. GNRs@QMSN completely eradicated bacterial infections and accelerated wound healing under laser irradiation. In addition, GNRs@QMSN demonstrated good biocompatibility *in vitro* and *in vivo*. Therefore, this therapeutic strategy combines the synergistic effects of adhesion, intrinsic and photothermal, provides a new approach for the treatment of deep bacterial biofilm infections.

Declaration of competing interest

The authors declare that they have no known competing financial interests or personal relationships that could have appeared to influence the work reported in this paper.

CRediT authorship contribution statement

Kaihang Sheng: Writing – original draft, Formal analysis, Data curation. **Yanshuai Wang:** Formal analysis, Data curation. **Siyuan Yin:** Formal analysis. **Xiuling Li:** Formal analysis. **Xinya Zhang:** Formal analysis. **Xiaowei Li:** Writing – review & editing, Supervision. **Dechao Niu:** Writing – review & editing, Supervision, Project administration, Funding acquisition, Conceptualization.

Acknowledgments

This work was financially supported by the National Natural Science Foundation of China (No. 32371406), Key Program of National Natural Science Foundation of China Regional Joint Funds (No. U24A20376), Program of Shanghai Academic/Technology Research Leader (No. 22XD1421100), Fundamental Research Funds for the Central Universities, and the 111 project (No. B14018), the Natural Science Foundation of Shandong Province (No. ZR2025MS825) and the China Postdoctoral Science Foundation (No. 2024M761775).

Supplementary materials

Supplementary material associated with this article can be found, in the online version, at doi:10.1016/j.cclet.2025.111852.

References

[1] H. Li, J.A. Jiang, X.Y. Lv, et al., Small 20 (2024) 2402723.
[2] Y. Xu, J.A. Jiang, X.Y. Lv, et al., Chem. Eng. J. 479 (2024) 147645.
[3] X.Y. Ren, C.Y. Yang, L. Zhang, et al., Nanoscale 11 (2019) 11830–11838.
[4] Y.L. You, Y.X. Zhu, J.J. Jiang, et al., J. Am. Chem. Soc. 145 (2023) 13249–13260.
[5] M. Ge, Z.S. Ruan, Y.X. Zhu, et al., Sci. Adv. 10 (2024) eadp3976.
[6] W. Tang, Y. Fang, L.H. Xie, et al., Adv. Healthc. Mater. 14 (2025) 2405009.
[7] Y. Lu, R. Xu, W. Liu, et al., J. Mater. Chem. B 12 (2024) 5111–5127.
[8] Z.Y. Liang, W.K. Liu, Z.Q. Wang, et al., Acta Biomater. 143 (2022) 428–444.
[9] J.J. Zhang, H.Y. Guo, M. Liu, et al., Exploration 4 (2024) 20230087.
[10] Y.L. You, X. Yu, J.J. Jiang, et al., Nat. Commun. 16 (2025) 2836.
[11] D.Y. Zhao, J.L. Feng, Q.S. Huo, et al., Science 279 (1998) 548–552.
[12] N.Q. Yin, X.L. Wang, T.H. Yang, et al., Ceramics Int. 47 (2021) 8271–8278.
[13] Y. Wang, H.C. Gu, Adv. Mater. 27 (2015) 576–585.
[14] Y. Tao, E.G. Ju, J.S. Ren, et al., Adv. Mater. 27 (2015) 1097–1104.
[15] C.Y. Cao, W. Ge, J.J. Yin, et al., Small 16 (2020) 2000436.
[16] Y.J. Xin, Z.Y. Guo, A.J. Ma, et al., Chem. Eng. J. 451 (2023) 138782.
[17] T. Niimura, Y. Kurokawa, S. Horiike, et al., Phys. Rev. B 102 (2020) 094411.
[18] H.W. Fan, M.H. Peng, I. Strauss, et al., Nat. Commun. 12 (2021) 38.
[19] A. Titova, C. Fowley, E. Clifford, et al., Sci. Rep. 9 (2019) 4020.
[20] J.L. Wang, Y.X. Wang, L. Xu, et al., Carbohydr. Polymers 181 (2018) 19–26.
[21] W.J. Yang, G.L. Huang, J. Mol. Struct. 1285 (2023) 135480.
[22] G.Y. Qian, Y.W. Li, H.B. Chen, et al., Nat. Commun. 14 (2023) 6048.
[23] Q.L. Li, X.B. Zhang, C. Guo, et al., Materials 17 (2024) 1754.
[24] Y. Chen, W. Wei, Y. Zhao, et al., Materials 16 (2023) 7036.
[25] D.C. Niu, Z. Ma, Y.S. Li, et al., J. Am. Chem. Soc. 132 (2010) 15144–15147.
[26] L.M. Qin, D.C. Niu, Y. Jiang, et al., IJN 14 (2019) 1519–1532.
[27] T.C. Chou, Pharmacol. Rev. 58 (2006) 621–681.
[28] X.Y. Wang, M. Liu, C.J. Yu, et al., Mol. Biomed. 4 (2023) 49.
[29] J.G. Li, G.Y. Pan, G.V. Zyryanov, et al., ACS Appl. Mater. Interfaces 15 (2023) 40864–40876.
[30] E.A. Saverina, N.A. Frolov, O.A. Kamanina, et al., ACS Infect. Dis. 9 (2023) 394–422.